





Molecular Dynamics Study on Quartz-Indenter Shape and Depth Effects in Epoxy Interfacial Mechanics

Pengchang Wei¹ D | Zhen-Yu Yin² | Pierre-Yves Hicher³ | Yuanyuan Zheng⁴

¹Department of Civil and Environmental Engineering, The Hong Kong Polytechnic University, Hung Hom, Kowloon, Hong Kong, China | ²Department of Civil and Environmental Engineering, Research Institute for Land and Space (RILS), The Hong Kong Polytechnic University, Hung Hom, Kowloon, Hong Kong, China | ³Research Institute of Civil Engineering and Mechanics (GeM), UMR CNRS 6183, Ecole Centrale de Nantes, Nantes, France | ⁴School of Civil Engineering, Sun Yat-Sen University & Southern Marine Science and Engineering Guangdong Laboratory (Zhuhai), Zhuhai, China

Correspondence: Zhen-Yu Yin (zhenyu.yin@polyu.edu.hk)

Received: 1 April 2025 | Revised: 12 May 2025 | Accepted: 31 May 2025

Funding: This work was financially supported by the Research Grants Council (RGC) of Hong Kong Special Administrative Region Government (HKSARG) of China (Grant No.: N_PolyU534/20, 15217220), Research Centre for Nature-based, Urban Infrastructure Solutions (Grant No.: P0053045) of The Hong Kong Polytechnic University, and the Project of RCRE (Grant No.: 1-BBEM) of The Hong Kong Polytechnic University.

Keywords: FRP-soil interface | indentation depth | indenter effect | molecular dynamics | nanoindentation | nanoscractching

ABSTRACT

The interfacial mechanical behavior between epoxy and quartz at the microscale remains inadequately understood. The quartz-indenter shape and indentation depth (h_c) effect on epoxy interfacial mechanical behavior has been investigated through molecular dynamics (MD) simulation of nanoindentation and nanoscratching. This work employs two Vickers-type and four spherical indenters with varying radii (R) under different h_c conditions, revealing the fundamental deformation mechanisms at the microscale. The reduced modulus and Young's modulus of epoxy resin obtained from MD simulations align well with experimental results. Key findings include: (1) during MD nanoindentation, the elastic-plastic deformation of epoxy and the indentation force increased with rising R and h_c , due to the enhanced interfacial interactions between epoxy and quartz. (2) A negative indentation force was observed during the unloading stage, attributed to adhesion effects. (3) In MD nanoscratching, the forces in the y- and z-directions increased with rising R and h_c , which was due to a greater contact zone and elastic-plastic deformation. (4) The friction coefficient could increase with rising indentation depth, exceeding 1.0 at $h_c/R > 0.75$. (5) The classic Coulomb's law of friction was not applicable at the microscale or nanoscale. These results provide a foundation for developing interfacial models at the macroscopic scale for engineering applications.

1 | Introduction

Fiber reinforced polymer (FRP) composites have gained significant traction across a variety of fields, including marine engineering, construction, aerospace, civil, and hydraulic engineering [1], due to their remarkable properties, such as high strength-to-weight ratio, corrosion resistance, electromagnetic transparency, and ease of handling. In geotechnical engineering, the understanding of the interfacial properties between FRP

composites and soil is crucial for ensuring the stability and integrity of the structure-soil system [2, 3]. Moreover, epoxy resin is the core matrix material of FRP. Modifying epoxy resin with nanomaterials (e.g., nano-quartz and its size of 1–100 nm) to improve its strength and toughness properties is one of the current research focuses in this topic [4]. For this purpose, it is essential to investigate the interfacial mechanical properties of epoxy and quartz at the microscale to obtain an understanding of the physical mechanisms governing their mechanical behavior.

This is an open access article under the terms of the Creative Commons Attribution License, which permits use, distribution and reproduction in any medium, provided the original work is properly cited.

@ 2025 The Author(s). International Journal for Numerical and Analytical Methods in Geomechanics published by John Wiley & Sons Ltd.

Most existing studies have concentrated on examining the macroscopic mechanical properties of epoxy and quartz mixtures through experimental methods [5, 6] and numerical analyses [7], such as direct shear and interfacial shear tests. These investigations have primarily addressed the characteristics of the mixtures themselves, often overlooking the critical interfacial interactions [4,8]. Consequently, the interfacial behavior between epoxy and soil remains insufficiently understood, especially at the microscale. Furthermore, the macroscopic properties of materials are profoundly affected by their micro-/nanoscale characteristics, where some factors (e.g., composition degradation, failure initiation, and microscopic mechanical behavior) play significant roles in determining overall performance [9, 10]. Therefore, investigating the mechanical properties at the microscale is crucial for gaining insights into the behavior of materials on a larger scale [11].

The molecular dynamics (MD) simulation method has effectively been used to study the interfacial mechanical behavior of materials, providing fundamental insights that are difficult to achieve experimentally [12–17]. To date, MD simulations have been successfully employed to investigate the adhesion [18], interfacial friction [2], and creep [3] behavior of the epoxy-quartz interface. However, there has been limited research focusing on their interfacial interactions at the microscale.

Nanoindentation and nanoscratching techniques are powerful tools for investigating the tribological and mechanical properties of materials at the microscale ($\sim 10^{-9}$ m) [19-22]. In both MD simulations and experimental studies, previous research has primarily focused on pure epoxy resin [23], quartz [24], and mixtures of epoxy composites with other modified materials [25, 26], such as nanoclay and fumed silica. Additionally, the nanoscratching behavior of epoxy/MWNT nanocomposites [27], polymer nanocomposites [28], and other materials [29] has been explored. These studies have demonstrated that factors such as loading rate, temperature, indenter shape and size, and indentation depth significantly influence the interfacial mechanical properties observed in nanoindentation and nanoscratching. Recently, the effect of loading rate on the interfacial mechanical behavior of epoxy-quartz systems was examined using MD nanoindentation and nanoscratching [30]. However, this research did not consider the effects of quartz shape, as well as the holding and unloading stages during the nanoindentation process. To our knowledge, the interfacial mechanical behavior between epoxy and quartz has been rarely studied using MD nanoindentation and nanoscratching.

To address this gap, this study investigates the effects of quartz-indenter shape and nanoindentation depth effects on epoxy interfacial mechanics behavior through MD nanoindentation and nanoscratching. This work aims to: (1) analyze the effects of different indenter shapes and sizes on FRP-soil interfacial behavior at the microscale; (2) reveal the elastic-plastic deformation mechanisms of epoxy resin during nanoindentation and nanoscratching processes, and their interactions with quartz indenters; and (3) provide an atomistic understanding of FRP-soil interfacial behavior.

2 | Simulation Procedure

2.1 | System Setup

Figure 1 shows the epoxy resin–quartz system used for MD nanoindentation and nanoscratching, where the dimensions of the whole system are 144.381 Å \times 288.559 Å \times 180.26 Å. Six different quartz indenters were established via VMD software to study the effect of the indenter shape and size, such as Vickers-type indenters (i.e., pyramid-0°, pyramid-45° indenters, see Figure 2a) and spherical indenters (i.e., spherical indenters with different radii of 10, 14.5, 20, and 25 Å, see Figure 2b). The crystal structure of quartz indenters contained three atoms (i.e., Si, O, and H), where the hydrogen atoms are at the outermost edge faces of the molecular model due to the oxidation effect. Moreover, all quartz indenters were set as a rigid body during all MD simulations, because the hardness of the nanoindenter (e.g., diamond) used in previous nanoindentation experiments was usually very high.

The epoxy substrate containing 228,000 atoms was composed of 4000 diglycidyl ether of bisphenol A (DGEBA) as an organic compound and 2000 *m*-phenylenediamine (mPDA) as a curing agent, where its conversion percentage of 84% was obtained through the cross-linking reaction between the epoxy group and an amino group at 600 K. As shown in Figure 1a, there are three layers (i.e., Newtonian layer, Thermostat layer, and Boundary layer) for the epoxy substrate, and their control methods at each layer and the accuracy verification of this epoxy model are detailed in our prior work [30]. Furthermore, a periodic boundary along the *x*- and *y*-directions was applied, and the vacuum over 40 Å was set the nonperiodic boundary along the *z*-direction.

2.2 | Force Fields

The polymer consistent force field (PCFF) and consistent valence force field (CVFF) have been successfully employed for organic compounds (e.g., epoxy system [3, 31]) and inorganic materials (e.g., quartz [3, 32]), respectively. Thus, the PCFF and CVFF were employed for the epoxy substrate and the quartz indenter in this study, respectively. Moreover, their formulations are displayed in Equations (S1) and (S2) (which could be found in the Supporting Information).

It is worth noting that the nonbonded interaction between quartz and epoxy contained the Coulomb electrostatic and van der Waals interactions, while the van der Waals interaction terms in PCFF and CVFF were different, such as the standard 9–6 Lennard–Jones (LJ) potential for PCFF and 12–6 LJ potential for CVFF. Thus, as shown in Table S1, based on 9–6 LJ parameters of each atom in the epoxy system, its corresponding 12–6 LJ potential parameters could be obtained through a fitting method, which is proposed in our prior work [30]. Thereafter, the nonbonded interaction between epoxy and quartz could be calculated by the same 12–6 LJ potential, where σ_{ij} and ε_{ij} between atom i and atom j were calculated by mixing Lorentz–Berthelot's law [33] (i.e., Equations 1, 2).

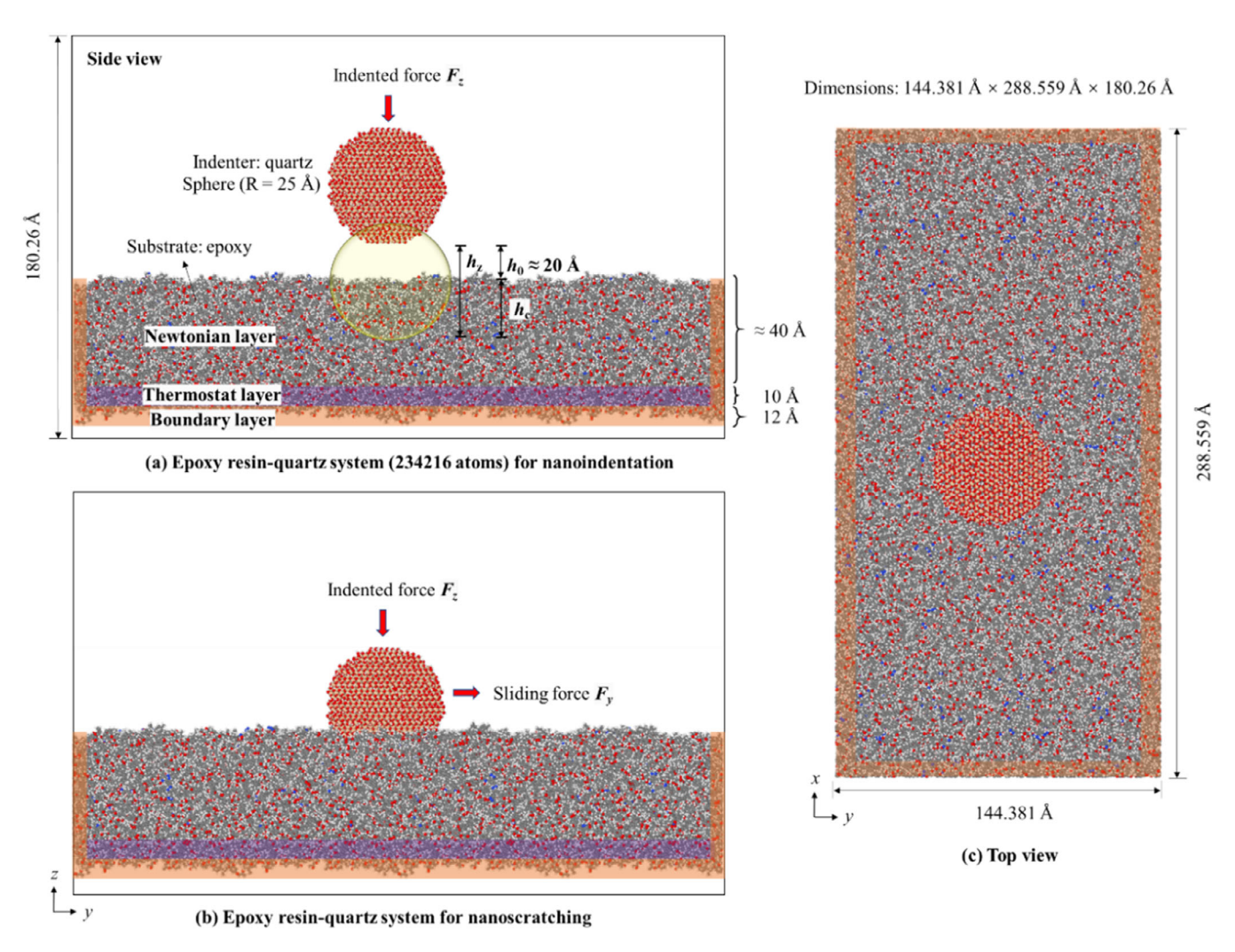


FIGURE 1 Epoxy resin–quartz system for (a) molecular dynamics (MD) nanoindentation and (b) nanoscratching simulation, where the quartz model is set as an indenter, and the epoxy as a substrate. (c) Top view of the whole system. Note that h_c , h_z , and h_0 are the indentation depth (i.e., contact depth between the epoxy substrate and the quartz indenter), displacement of quartz indenter along the z-direction, and initial distance between epoxy and quartz, respectively.

$$\sigma_{ij} = \frac{\sigma_i + \sigma_j}{2} \tag{1}$$

$$\varepsilon_{ij} = \sqrt{\varepsilon_i \varepsilon_j} \tag{2}$$

2.3 | MD Nanoindentation and Nanoscratching Simulations

All MD simulations were conducted using the LAMMPS code [34]. Table 1 displays some setting algorithms and methods for all MD simulations in this study, and more detailed simulation parameters are shown in the section "Code availability". The velocity-Verlet algorithm was used to integrate motion equations. The cutoff radius for the van der Waals forces and long-range electrostatic interactions using the PPPM method was 10 and 8.5 Å, respectively. A time step of 1.0 fs and a temperature of 300 K were maintained throughout all MD simulations.

The whole system was equilibrated with the Langevin thermostat at 300 K and NVE ensemble for 1.0 ns, the quartz indenter kept still during this process. Figure 3 shows the evolution of total

energy and temperature with time for the pyramid-0° quartz indenter–epoxy system during equilibration, indicating that the whole system reached equilibrium after 600 ps.

As shown in Figure 4, all MD nanoindentation simulations for the epoxy–quartz system are divided into three stages: loading, holding, and unloading stages. (1) The loading stage was conducted using displacement-controlled mode, where the quartz indenter moved toward the epoxy substrate along the z-direction with a loading rate of 1.0 Å/ps. The final displacement of the quartz indenter along the z-direction (h_z) was set at 45 Å, and the corresponding final indentation depth (h_c) was 25 Å (Figure 4a). (2) During the holding stage, the quartz indenter remained stationary, and the epoxy substrate could further equilibrate (Figure 4b). (3) During the unloading stage, the quartz indenter moved away from the epoxy substrate (Figure 4c).

The quartz–epoxy system with different target indentation depths (h_c : 4, 7, 10, 16, 22, and 25 Å) could be obtained during the loading stage of MD nanoindentation. Thereafter, as shown in Figure 1b, MD nanoscratching simulations were conducted,

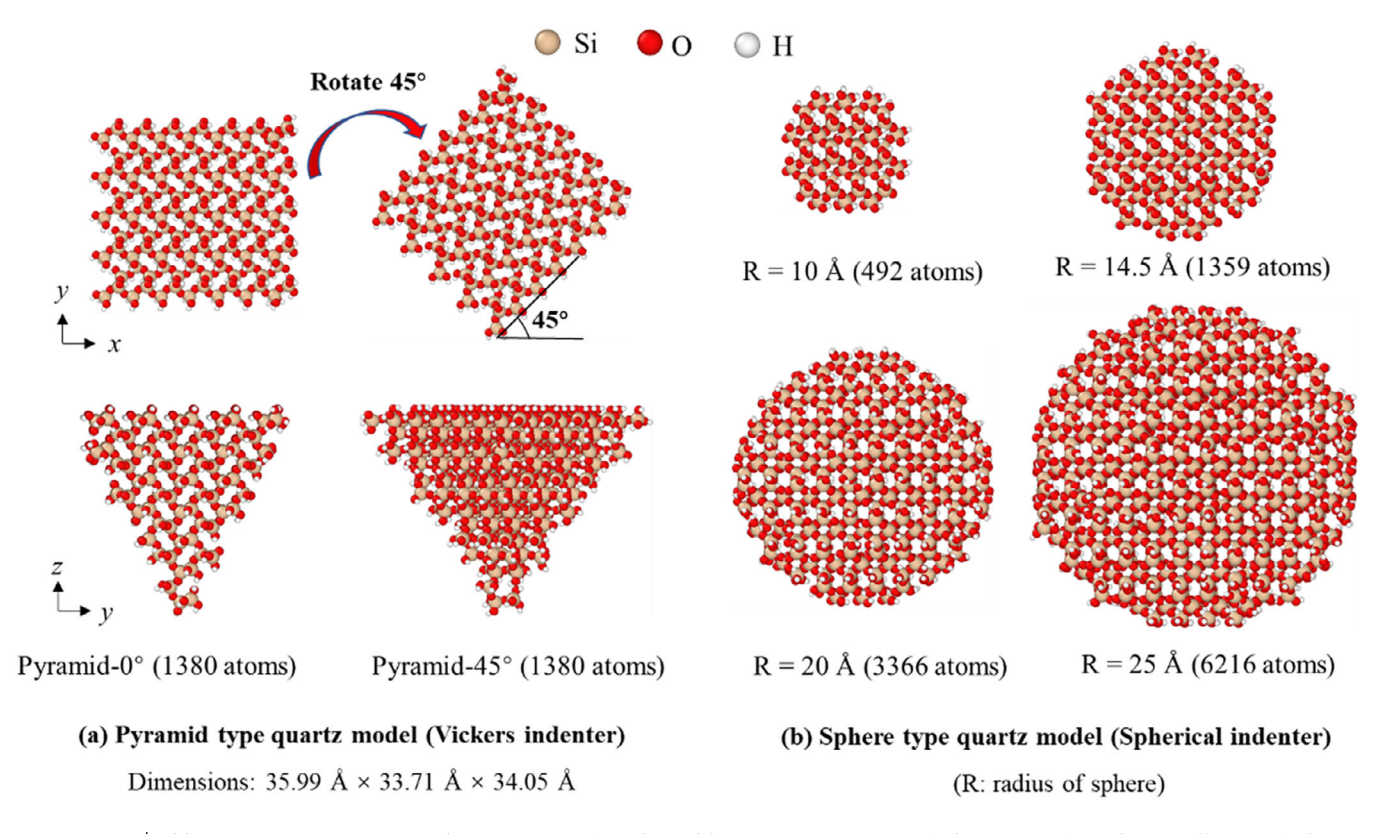


FIGURE 2 | (a) Pyramid type quartz model (Vickers-type indenter) and (b) sphere type quartz model (spherical indenter) with different radii (10–25 Å).

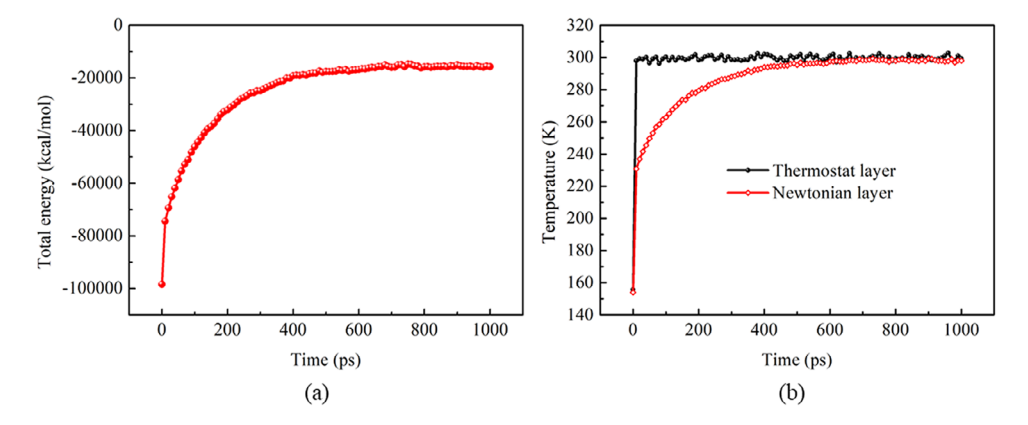


FIGURE 3 | Evolution of total energy and temperature with time for pyramid-0° quartz indenter-epoxy system during equilibration stage of 1.0 ns.

(3)

where the quartz indenter slid along the y-direction using displacement-controlled mode at a sliding velocity of 1.0 Å/ps. All nanoscratching simulations slid along the sliding y-direction until the calculation was terminated due to excessive interactions between atoms, resulting in different sliding distances obtained in different simulation groups.

Physical Quantity Analysis

The indentation depth (i.e., contact depth, h_c) was calculated by the following equation:

$$h_{\rm c} = h_z - h_0 = \Delta h \times n_{\rm step}^{\rm loading} - h_0 \tag{3}$$

where h_c , h_z , and h_0 are the indentation depth (corresponding to the depth of quartz indenter into the epoxy resin substrate), the displacement of the quartz indenter along the z-direction, and the initial distance between epoxy and quartz ($h_0 = 20 \text{ Å}$), respectively. $n_{\mathrm{step}}^{\mathrm{loading}}$ is the number of loading steps, where the timestep is 1.0 fs. Δh is the loading rate (i.e., displacement rate) of the quartz indenter, equal to 1.0 Å/1000 steps (i.e., 1.0 Å/ps =100 m/s).

The projected contact area (A_c) of the pyramid-type quartz indenter (Figure 5a) at h_c could be obtained by Equations (4–6).

$$d_1 = 2h_c \times \tan\varphi \tag{4}$$

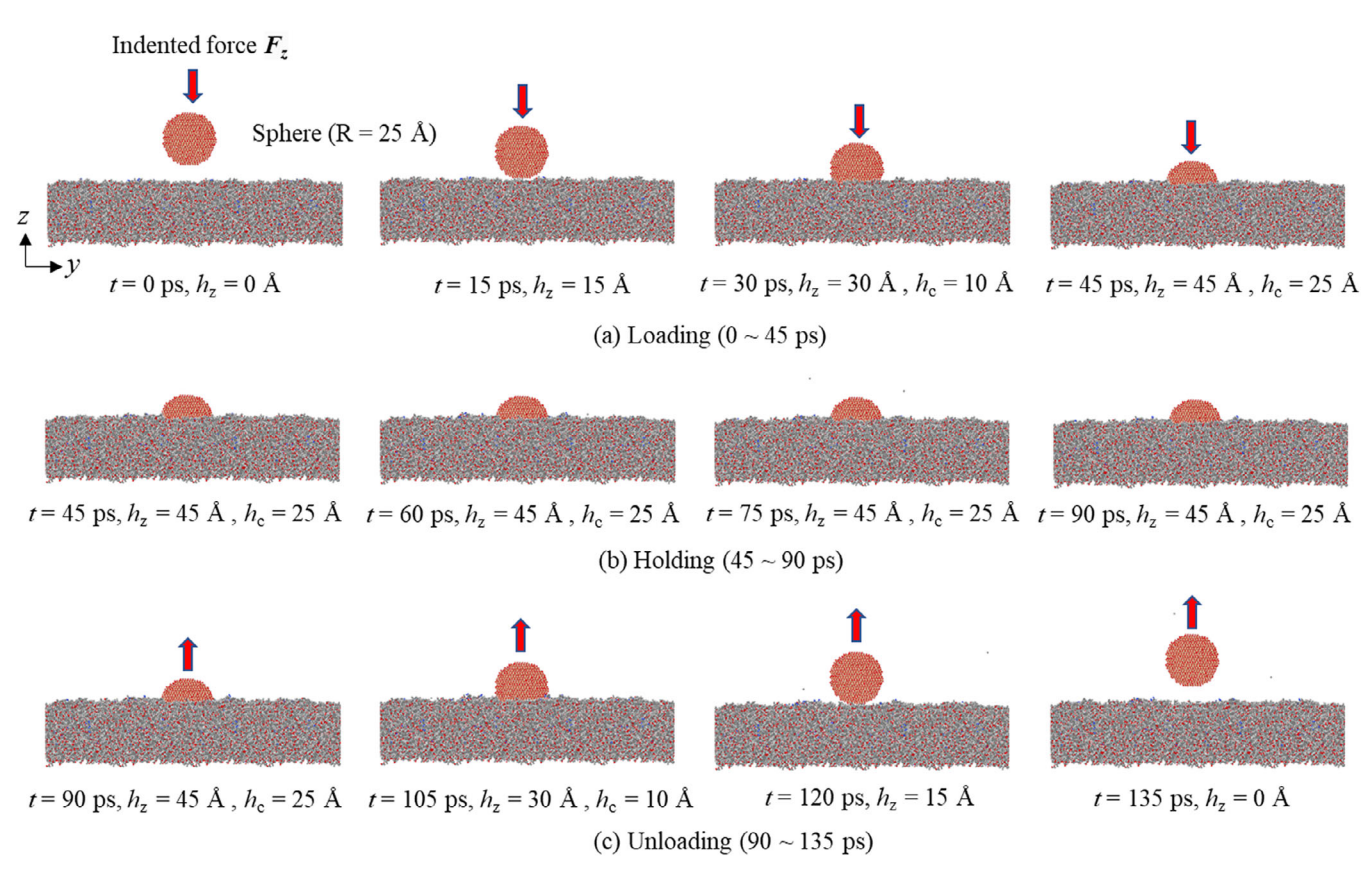


FIGURE 4 Molecular dynamics (MD) nanoindentation simulation process for epoxy–quartz system (R = 25 Å), including three stages: (a) loading, (b) holding, and (c) unloading stage.

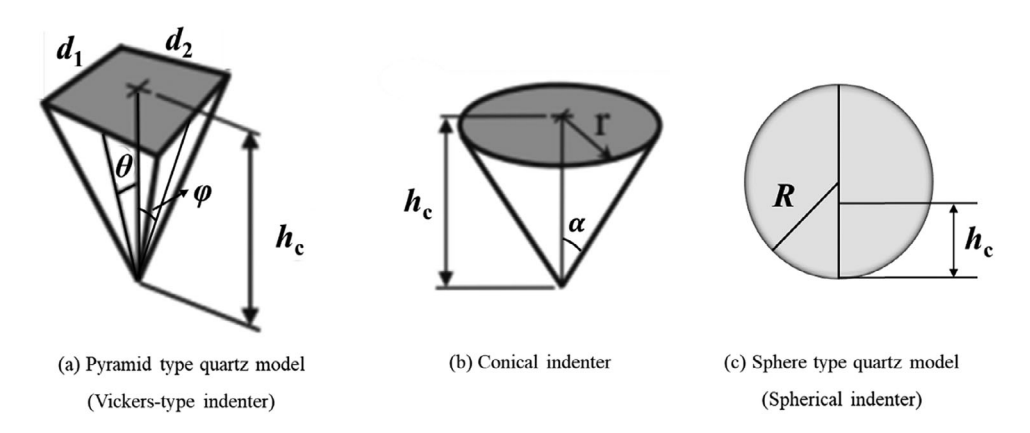


FIGURE 5 | Indentation parameters for (a) pyramid type quartz model (Vickers-type indenter), conical indenter, and sphere type quartz model (spherical indenter), modified from [35]. Note that d_1 , d_2 , φ , θ are corresponding length and angle in this quartz indenter, where φ and θ were set as 27.87° and 26.35°, respectively.

$$d_2 = 2h_c \times \tan\theta \tag{5}$$

$$A_{c} = d_{2} \times d_{1} = 4h_{c}^{2} \tan\varphi \tan\theta \tag{6}$$

For a conical indenter (Figure 5b), the relationship between the indentation force (P, alias F_z) and h_c followed Equation (7) [35]. It should be noted that the shape of the conical indenter was very similar to that of the Vickers-type indenter. Thus, Equation (7) was used to describe the relationship between the indentation

force (i.e., P or F_z) and h_c for Vickers-type indenter and was modified as Equation (8). E_r is the reduced modulus (alias indentation modulus) and is also applicable to various axisymmetric shapes of the indenter and elastic–plastic contact [36].

$$P = \frac{2E_{\rm r} \tan \alpha}{\pi} h_{\rm c}^2 \tag{7}$$

$$P = \frac{2E_{\rm r} \tan\left(\frac{\theta + \varphi}{2}\right)}{\pi} h_{\rm c}^{2} \tag{8}$$

TABLE 1 \mid Some setting algorithms and methods for all MD simulations in this study.

Setting algorithm and methods	Purpose/parameter
Three-dimensional periodic boundary conditions	Simulating the behavior of large systems and improving computational efficiency
Velocity-Verlet algorithm	Integrating the motion equations
Lennard–Jones potential model	Calculating the van der Waals interaction, and a cutoff radius of 10 Å
PPPM/TIP4P method	Calculating the long-range electrostatic interaction, and a cutoff radius of 8.5 Å, and the desired relative error in forces of 1e-4
Neighbor	1.0 bin
Time step	1.0 fs
Temperature	300 K

For spherical indenters (Figure 5c), based on Hertz contact theory [37], its projected contact area (A_c) and the relationship between the indentation force (P, alias F_z) and h_c are given by Equations (9) and (10), respectively [35].

$$A_{\rm c} = \pi \left(2Rh_{\rm c} - h_{\rm c}^{2} \right) \tag{9}$$

$$P = \frac{4}{3}E_{\rm r}R^{1/2}h_{\rm c}^{3/2} \tag{10}$$

The indentation hardness (H) represents the ability of the tested material to withstand contact loads [38] and is defined as the ratio of the maximum indentation force (P_{\max}) to the projected contact area (A_c) of the indenter as follows:

$$H = \frac{P_{\text{max}}}{A_{\text{c}}} \tag{11}$$

The relationship between Young's modulus (E) and $E_{\rm r}$ for the nanoindentation test is as follows:

$$\frac{1}{E_{\rm r}} = \frac{1 - v^2}{E} + \frac{1 - v_{\rm i}^2}{E_{\rm i}} \tag{12}$$

where E and v are the Young's modulus and Poisson's ratio of the substrate material (i.e., epoxy in this study), and E_i and v_i are the Young's modulus and Poisson's ratio of the indenter material (i.e., quartz in this study). Because the quartz indenter was set as a rigid body, E_i and v_i in Equation (12) are equal to ∞ and 0, respectively, and Equation (12) could be further expressed as follows:

$$\frac{1}{E_r} = \frac{1 - v^2}{E} \tag{13}$$

To quantify the plastic deformation behavior of atoms in the whole system, the shear strain (i.e., von Mises strain, η_i^{Mises})

of atoms was calculated using OVITO from the atomic Green–Lagrangian strain tensor (η) and the atomic deformation gradient tensor (J) for each atom, as shown in Equations (12, 13) [39].

$$\eta = \frac{J^{\mathrm{T}}J - I}{2} \tag{14}$$

 $\eta_{:}^{\mathrm{Mises}}$

$$= \sqrt{\eta_{xy}^2 + \eta_{xz}^2 + \eta_{yz}^2 + \frac{(\eta_{xx} - \eta_{yy})^2 + (\eta_{xx} - \eta_{zz})^2 + (\eta_{yy} - \eta_{zz})^2}{6}}$$
(15)

where η and J are the atomic Green–Lagrangian strain tensor and atomic deformation gradient tensor for each particle, respectively. η_i^{Mises} and η_i^{Vol} are the shear strain and volumetric strain of the atom. $\eta_{xx}, \eta_{yy}, \eta_{zz}, \eta_{xy}, \eta_{xz}$, and η_{yz} are the six components of strain for each atom.

3 | Results and Discussions

3.1 | MD Nanoindentation Behavior

3.1.1 | Effect of Indentation Depth

Figure 6a shows the evolution of the indentation force F_z with the indenter displacement h_z for pyramid-0° indenters, and Figure 7 displays the evolution of pairwise interaction energy and force with time for all systems. When h_{τ} varied between 0 and 20 Å, the pairwise interaction energy and force, as well as F_z were close to 0 due to the absence of contact between quartz indenter and epoxy substrate. During the loading stage (h_z rising from 20 to 45 Å), F_z gradually increased with rising h_z when the quartz indenter moved into the epoxy substrate, causing an increase in the elasticplastic deformation and damage to epoxy (Figure 8). Thereafter, during the holding stage ($h_z = 45 \text{ Å}$), although the position of the quartz indenter remained unchanged, the atom positions within the epoxy substrate could further adjust to achieve a more balanced state, so F_z decreased from a maximum value to a stable value. Finally, during the unloading stage (h_z reducing from 45 to 0 Å), F_z rapidly decreased to 0, then took negative values, and finally went back to 0, when the quartz indenter gradually moved out. It is worth noting that the negative value for F_z was attributed to the adhesive effect between epoxy and quartz, which has been verified in previous MD works [40, 41].

The pop-in point is an important phenomenon during nanoin-dentation, indicating significant structural deformation mechanism changes within the material [35]. The pop-in phenomenon is usually more common in crystalline materials [42, 43], such as metal, ceramic material, quartz, etc. However, as shown in Figure 6, the fluctuation in F_z is relatively significant (Figure 6a–d), so it is impossible to determine whether the pop-in point exists or not. The pop-in point did not exist in Figure 6e, f. Because epoxy resins are generally amorphous (noncrystalline) polymer materials, molecular chain movements and rearrangements in epoxy resins might be gradual rather than sudden. This finding was also found in nanoindentation experiments on epoxy resins from previous works [23, 25, 44], which investigated the effect of temperature and loading rate. As shown in Figure

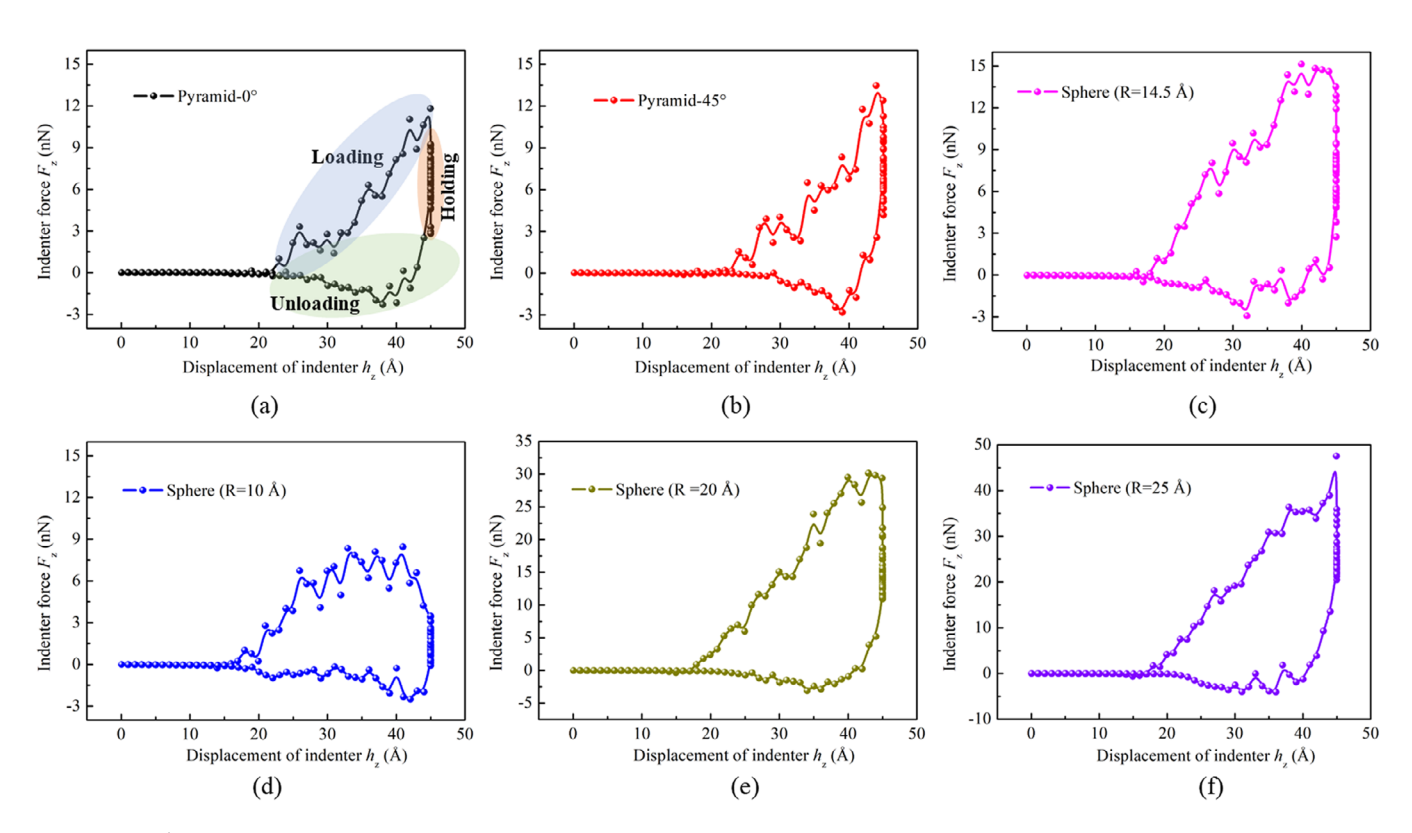


FIGURE 6 Evolution of indentation force (F_z) with displacement of the indenter (h_z) for various indenters: (a) pyramid-0°, (b) pyramid-45°, (c) sphere (R = 14.5 Å), (d) sphere (R = 10 Å), (e) sphere (R = 20 Å), and (f) sphere (R = 25 Å).

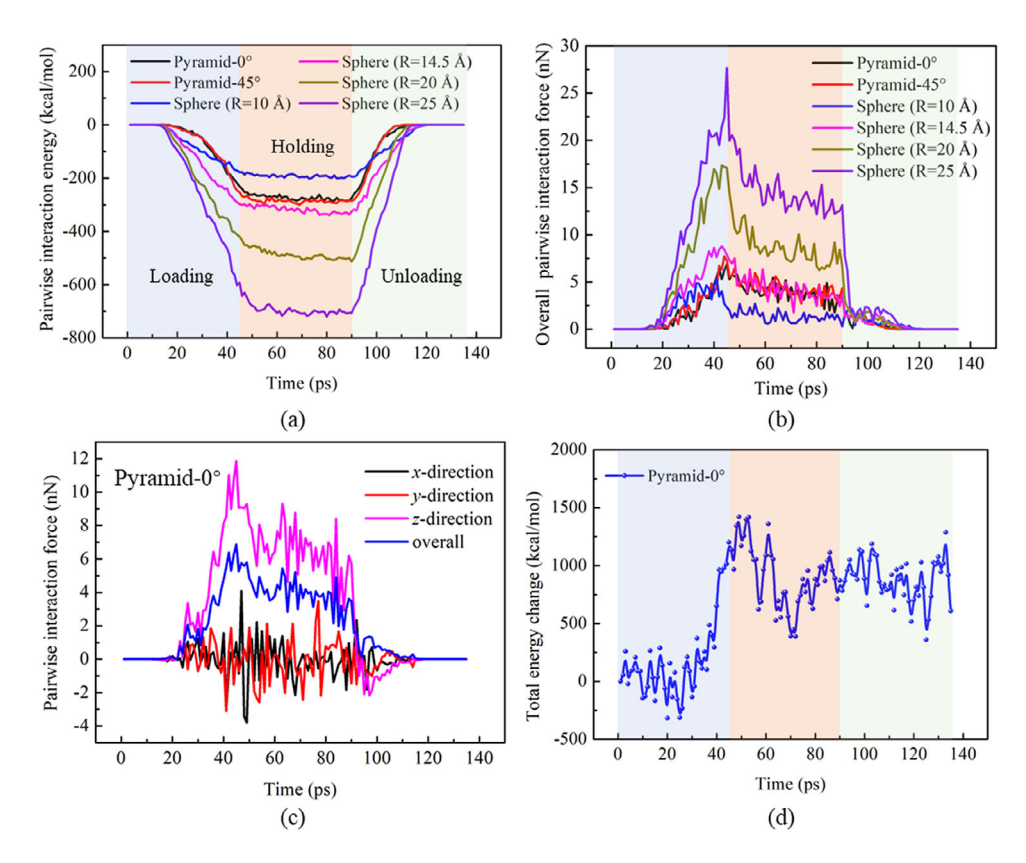


FIGURE 7 | Evolution of (a) pairwise interaction energy and (b) overall pairwise interaction force with time for all systems. (c) Relationship between pairwise interaction forces in different directions and time, where the overall pairwise interaction force is the squared mean of the three forces. (d) The evolution of total energy of pyramid-0° quartz indenter–epoxy system with time.

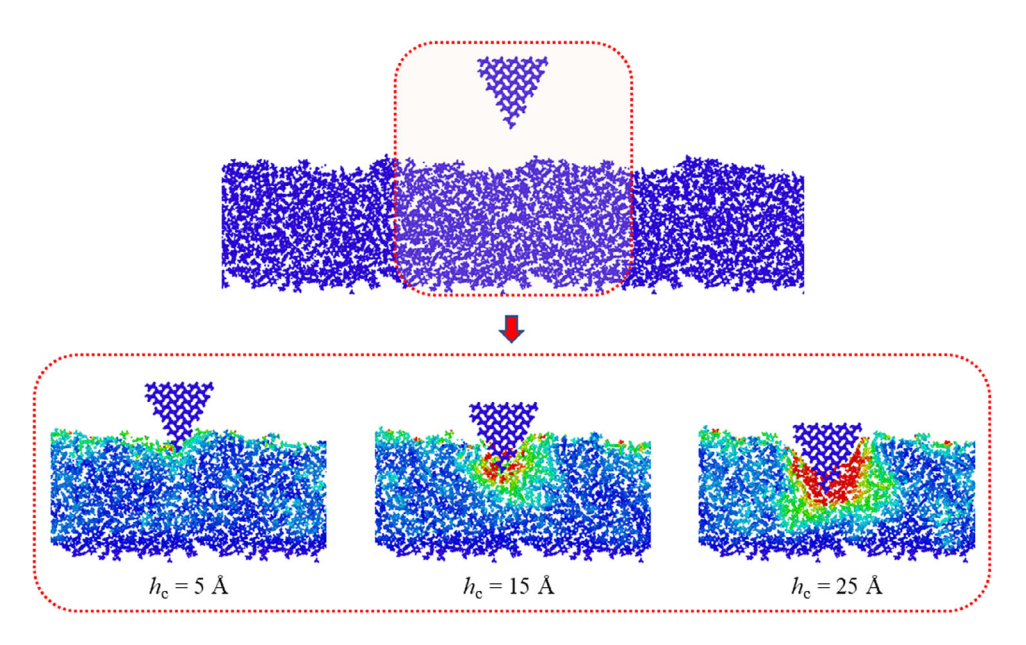


FIGURE 8 | Shear strain of atoms for pyramid-0° quartz indenter-epoxy system during loading stage.

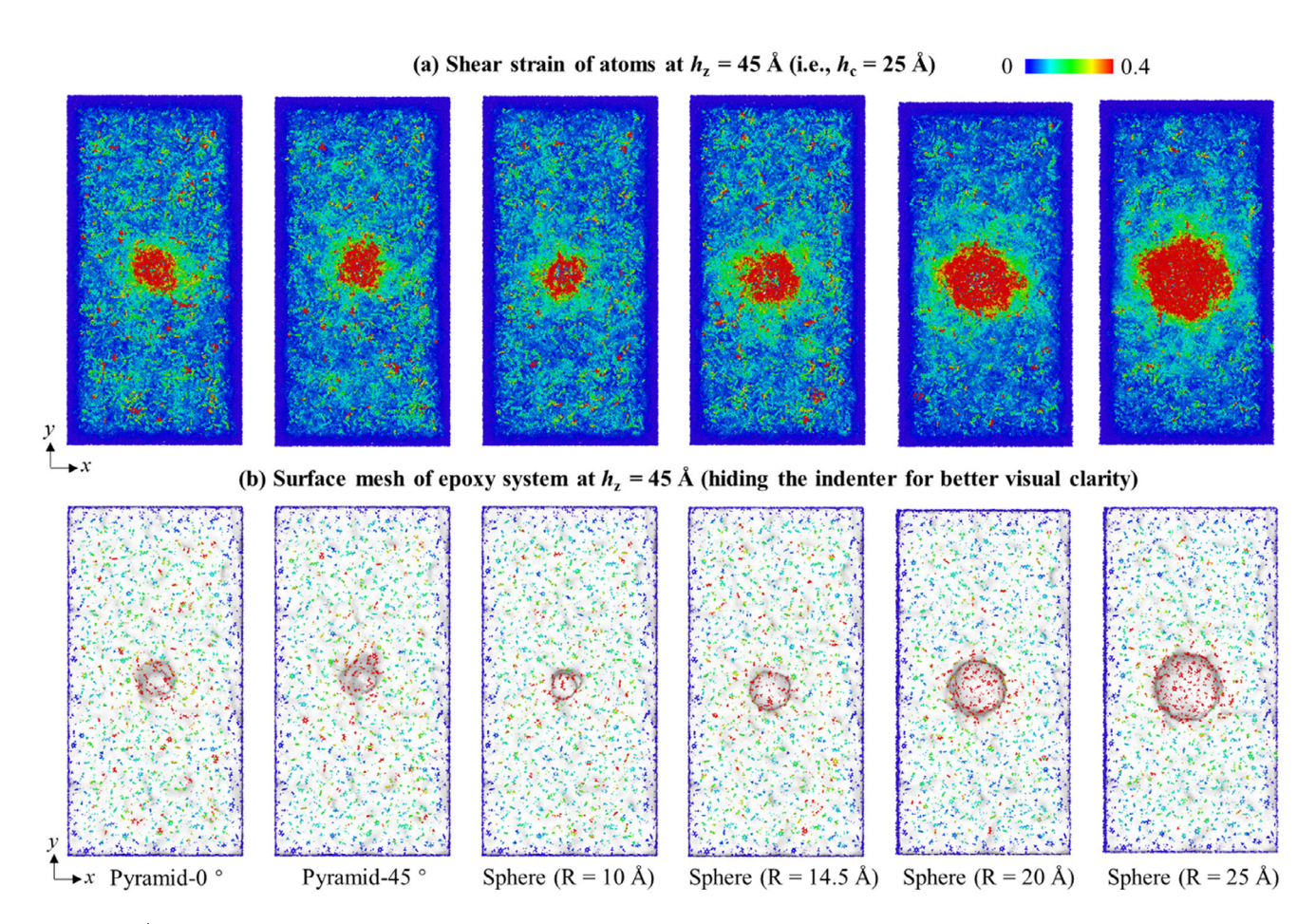


FIGURE 9 (a) Shear strain of atoms and (b) surface mesh of epoxy substrate for all systems; the quartz indenter is hidden for better visual clarity.

S1, the evolution of indentation load with indentation depth is different under different environmental factors, but there is no pop-in point in all curves, indicating that the existence of a pop-in point depends mainly on the properties of the material itself.

As shown in Figure 7b, c, the evolution of the overall pairwise interaction forces agrees well with that of F_z , while the pairwise interaction forces along the x- and y-directions fluctuate around 0, indicating that the z-direction interaction between the quartz indenter and the epoxy substrate has the dominant role. Figure 7d

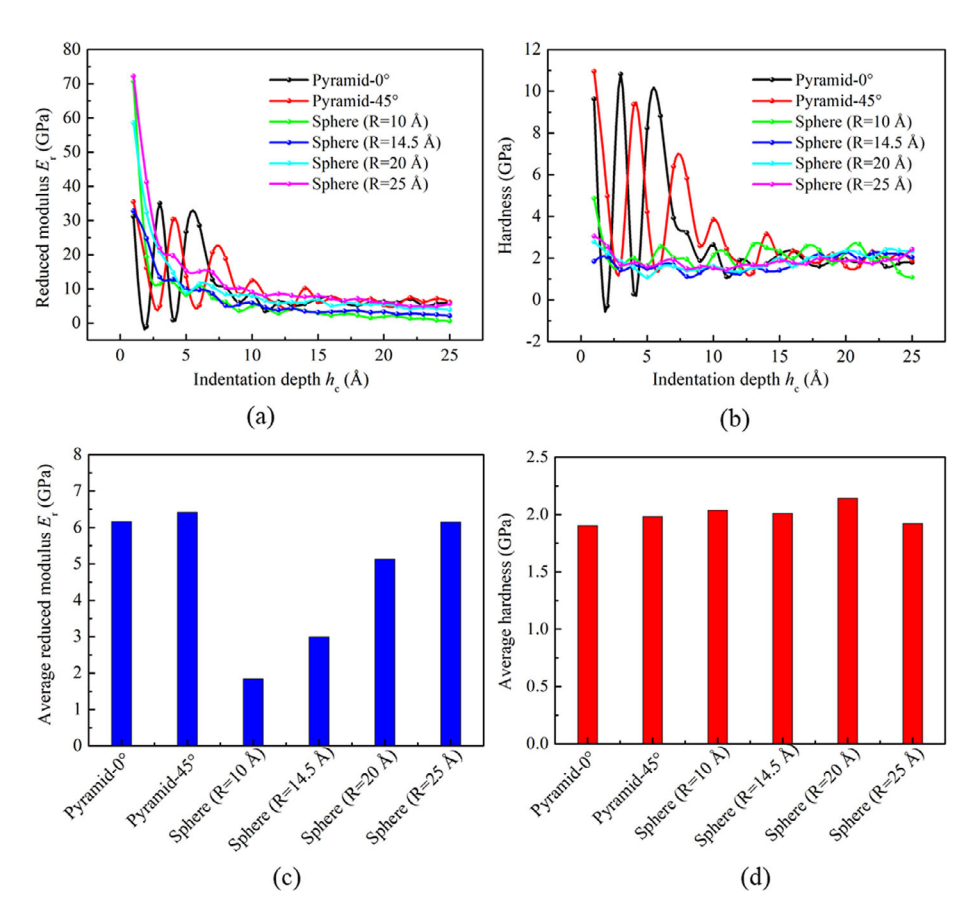


FIGURE 10 | Evolution of (a) reduced modulus (E_r) and (b) hardness (H) with indentation depth (h_c) for all systems. The (c) average reduced modulus and (d) average hardness were calculated based on the arithmetic average of the data for h_r in the interval 15–25 Å.

displays the evolution of the total energy change with time for the pyramid-0° quartz indenter–epoxy system, where the total energy gradually increases during the loading stage, indicating that the epoxy substrate has undergone irreversible plastic deformation, including energy dissipation and microstructural change (Figure 8). Thereafter, the total energy decreased with rising time during the holding stage, reflecting that the epoxy substrate was transitioning from plastic deformation to elastic recovery, including the given stress relaxation effects, such as the rearrangement of epoxy atoms.

3.1.2 | Effect of Indenter Shape and Size

As shown in Figure 6a, b, the evolution of F_z with h_z for pyramid-0° quartz indenter is close to the evolution of F_z for pyramid-45°, with the maximum F_z for pyramid-45° quartz indenter being slightly bigger. Due to the amorphous nature of epoxy, the arrangement and distribution of atoms vary in each direction. Moreover, as shown in Figure 6c–f, for various spherical quartz indenters, the higher the radius of the sphere, the higher the maximum value of F_z , the elastic–plastic deformation, and the damage of epoxy (Figure 9). This is because the interaction between the epoxy substrate and the quartz indenter gradually increased with a rising radius of the indenter (Figure 7a b).

Figure 10 displays the evolution of $E_{\rm r}$ and H with $h_{\rm c}$, calculated using Equations (8–11). For pyramid-0° and 45° quartz indenters, $E_{\rm r}$ and H fluctuated significantly at 0–10 Å of $h_{\rm c}$, and this

fluctuation gradually decreased with rising h_c (Figure 10a, b). For various spherical quartz indenters, E_r and H gradually reduced with increasing h_c from 0 to 10 Å, then remained unchanged for h_c between 15 and 25 Å (Figure 10b).

Figure 10c, d show that the reduced modulus and hardness are averaged based on their data at 15–25 Å of $h_{\rm c}$. The average reduced modulus for pyramid-0° quartz indenter was slightly smaller than that for pyramid-45°. For the spherical quartz indenter, the higher the radius, the higher the average reduced modulus, which is consistent with previous MD studies on amorphous alloy [40]. Moreover, for all quartz indenters, the average hardness of the epoxy substrate was close to 2 GPa (Figure 10d).

The average Poisson's ratio of the epoxy substrate used in this work obtained by uniaxial tension was 0.377, which agreed well with previous experimental results, giving values between 0.32 and 0.44 [45]. Thereafter, Young's modulus of the epoxy resin could be calculated by Equation (13). As shown in Table 2, the epoxy–quartz model established in this work could be validated by comparing $E_{\rm r}$ and E values reported in previous studies, which shows that $E_{\rm r}$ and E values in this MD simulation agree well with experimental results. However, it was noted that the hardness H of the epoxy resin obtained in MD simulations was one order of magnitude higher than its experimental value [26, 44, 46], which might be due to the size effects, defects and interface effects of experimental materials, the type of applied force field, etc. Many MD nanoindentation simulation mechanisms of the epoxy resin remained unclear and were worth further investigation.

TABLE 2 Reduced modulus (E_r) , Young's modulus (E), and indentation hardness (H) of epoxy resin in this work and similar materials (various epoxy resin composites) in previous studies.

Species	Methods	Value (GPa)	Notes
work Nanoi experi	MD results in this work	1.84-6.17	Epoxy resin at the loading rate of 1.0 Å/ps under various indenter
	Nanoindentation experiments in previous works	4.78–5.35	Epoxy resin at different loading rates of 0.25–6.0 mN/s [44]
		1.5–7.5	Nanoclay/epoxy composite at 40°C [25]
		4.0-7.1	Epoxy composite with 0%-5% CNF [46]
E	MD results in this work	1.58–5.29	Calculated by Equation (13)
Various experiments in previous works	Various experiments in previous works	2.21–2.72	DGEBA epoxy networks (containing DGEBA/D230, DGEBA/TETA, DGEBA/TEPA) through dynamic mechanical analysis experiments [47]
		3.5 (unmodified epoxy resin), 3.85 (epoxy + 8.5% nanofiller)	A DGEBA-based epoxy resin through the tensile test [4]
		2.83	Matrix epoxy Epon 862 [48]
		3.441–4.601 (DGEBA/AGE), 3.441–6.293 (DGEBA/GMA)	Epoxy resin composite by ultrasonic velocity Measurement [49]
		3.3 ± 0.12 (uniaxial tension), 3.9 ± 0.12 (nanoindentation)	Epoxy resin through uniaxial tension and nanoindentation test [26]
		3.76 (0 wt%), 3.49 (0.5 wt%), 3.47 (1.0 wt%)	Epoxy resin with 0.78 wt% polyaniline added by 0–1.0 wt% ZnO nanoparticles using nanoindentation test [50]
Н	MD results in this work	1.90-2.04	See Figure 10d
	Nanoindentation experiments in previous works	0.26-0.67	Epoxy composite with 0%–5% CNF [26, 44, 46]
		0.26-0.276	Epoxy resin at different loading rates of 0.25–6.0 mN/s [44]
		0.256-0.318	Epoxy reinforced nanocomposites with fumed silica of 0%–3% [26]

AGE, allyl glycidyl ether; CNF, carbon nanofiber; D230, Jeffamine D230; DETDA, diethyltoluenediamine; DGEBA, diglycidyl ether of bisphenol A; EPON862, bisphenol F diglycidyl ether; GMA, glycidyl methacrylate; mPDA, *m*-phenylenediamine; TEPA, tetraethylenepentamine; TETA, triethylenetetramine.

3.2 | MD Nanoscratching Behavior

3.2.1 | Effect of Indentation Depth

To understand the effect of $h_{\rm c}$ on MD nanoscratching behavior, Figure 11 shows the evolution of the forces on a spherical quartz indenter ($R=14.5\,$ Å) with the sliding distance for different $h_{\rm c}$. The forces along the y- and z-directions were greater than the force along the x-direction, which fluctuated around 0. Because the quartz indenter slid along the y-direction during the nanoscratching process, causing less impact in the x-direction. Moreover, the force along the three directions fluctuated with the sliding displacement due to the heterogeneity of the epoxy.

As h_c increased, the contact zone between the quartz indenter and the epoxy expanded, leading to the greater elastic–plastic deformation of the epoxy and accumulation of more atoms in front of the indenter (Figure 12). Thus, the forces in the *y*- and *z*-directions could increase with rising h_c .

3.2.2 | Effect of Indenter Shape and Size

To explore the effect of indenter shape and size on MD nanoscratching behavior, Figure 13 displays the relationship between sliding force and sliding distance at $h_{\rm c}$ of 4 Å. The fluctuation amplitude and the average sliding force on the spherical indenter $(R=14.5~{\rm \AA})$ were greater than those on the pyramid indenter-0° and 45° (Figures 13a–c, 14a). Moreover, for the spherical quartz indenter, the higher the radius of the spherical quartz indenter, the higher the absolute value of the average sliding force (Figure 14a). This result is significantly related to the contact area between the quartz indenter and the epoxy substrate (Figure 15), the indenter force (F_z) , and the deformation of the epoxy substrate.

As shown in Figures 13 and 14b, the evolution of the force with the sliding distance and the average sliding force for pyramid indenter-0° and 45° are very close, due to the same contact area between the quartz indenter and the epoxy substrate at the same

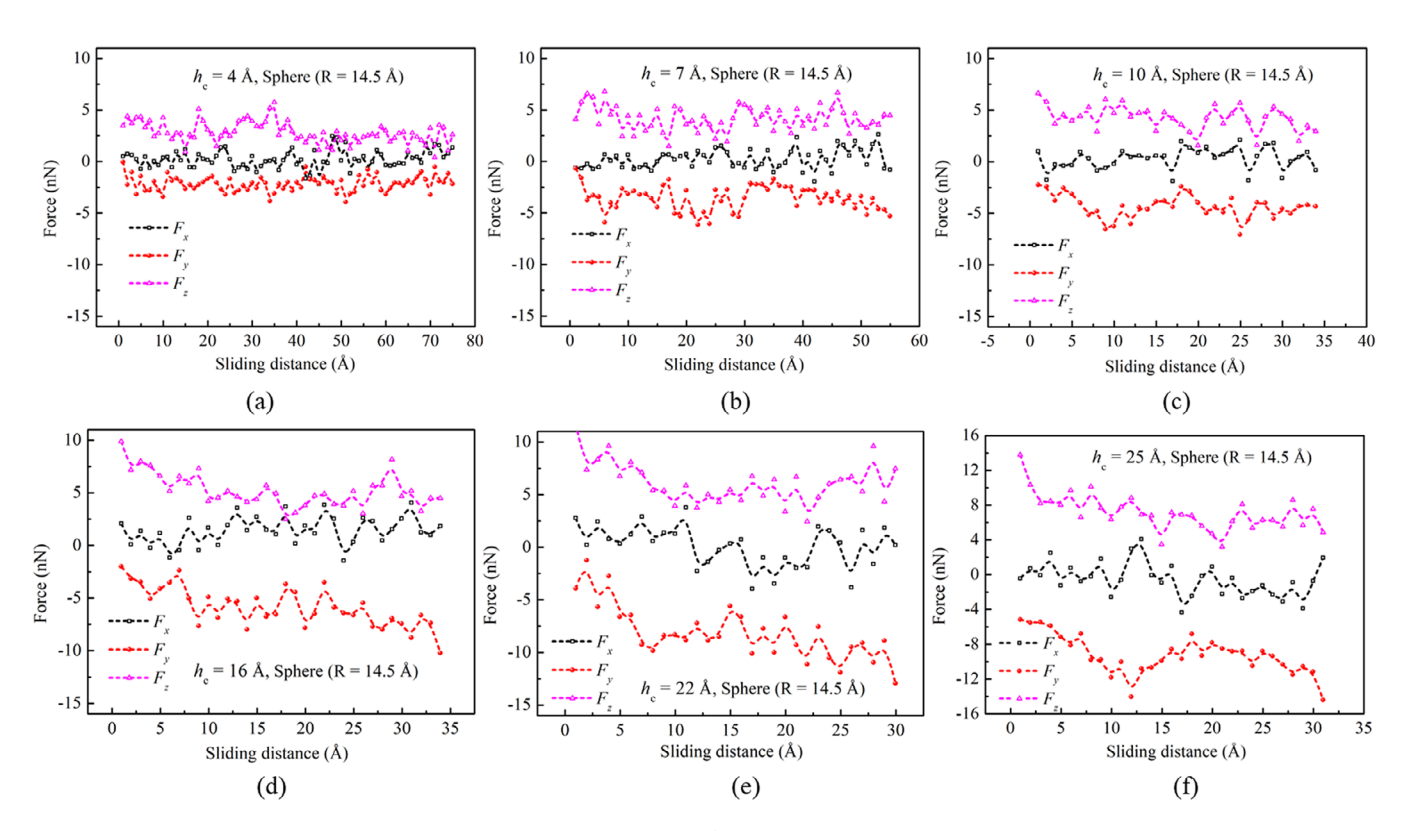


FIGURE 11 Evolution of forces on spherical quartz indenter (R = 14.5 Å) with sliding distance under different indentation depths (h_c) of (a) 4, (b) 7, (c) 10, (d) 16, (e) 22, and (f) 25 Å.

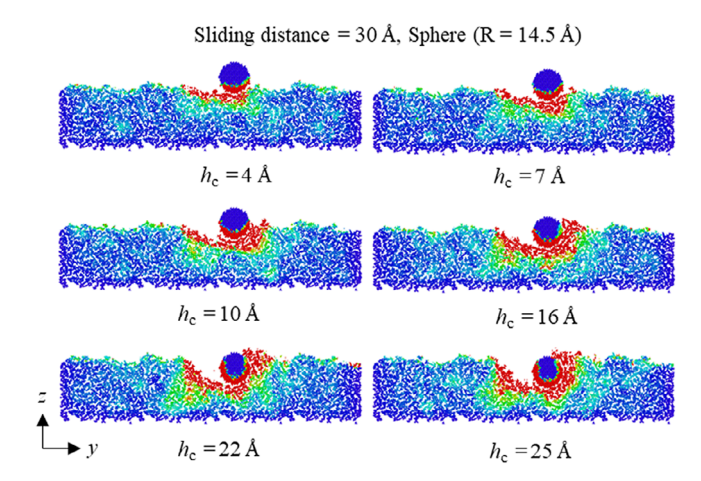


FIGURE 12 | Shear strain of atoms for spherical quartz indenter (R = 14.5 Å) and epoxy substrate at a sliding distance of 30 Å under different h_c .

 $h_{\rm c}$ of 4 Å. However, the average sliding force of all spherical quartz indenters was superior to that of the pyramid indenter-0° and 45° (Figure 14a), even for the spherical indenter (R=10 Å).

As shown in Figure 16, the relationship between forces along the y- and z-direction and h_c for all systems are significantly linear, while no obvious pattern is observed for F_z with the spherical quartz indenter (R = 10 Å) (see Figure 16d). Due to the relatively small radius of the spherical indenter (R = 10 Å), the whole indenter could completely penetrate into the epoxy substrate at h_c over 20 Å (Figure 17), causing a more complex interaction

between the quartz indenter and epoxy. Moreover, the higher the radius of the quartz indenter was, the higher the forces along the *y*- and *z*-directions were (Figure 16c–f).

3.3 | Discussion

3.3.1 | Friction Coefficient Evolution During Nanoscratching

The friction coefficient is a key parameter for understanding the resisting behavior of materials during friction or nanoscratching. Figure 17 shows the relationship between the friction coefficient and h_c/R for various spherical quartz indenters, where the friction coefficient is the ratio between F_y and F_z (see Figure 16). The friction coefficient for some spherical indenters at $h_c/R > 0.75$ was superior to 1.0 (Figure 17), which was consistent with previous MD nanoscratching studies [29, 51] and experimental friction/wear results [52-54]. Moreover, Jahanshahi et al. [55] investigated the mechanical properties of granular γ -alumina using experimental nanoscratching and found that the friction coefficient increased from 0.72 to 0.9 with the increase of indenter force and indenter depth (see Figure S2). As shown in Figure S2, it could be inferred that the friction coefficient could further increase with rising indenter force/depth, potentially exceeding 1.0.

According to the classic Coulomb's law of friction, the conventional friction coefficient of most materials is usually considered to be 0–1.0. However, in some specific cases, it could be higher than 1.0, such as silicone rubber (\sim 2.25) [52], rubber and flooring

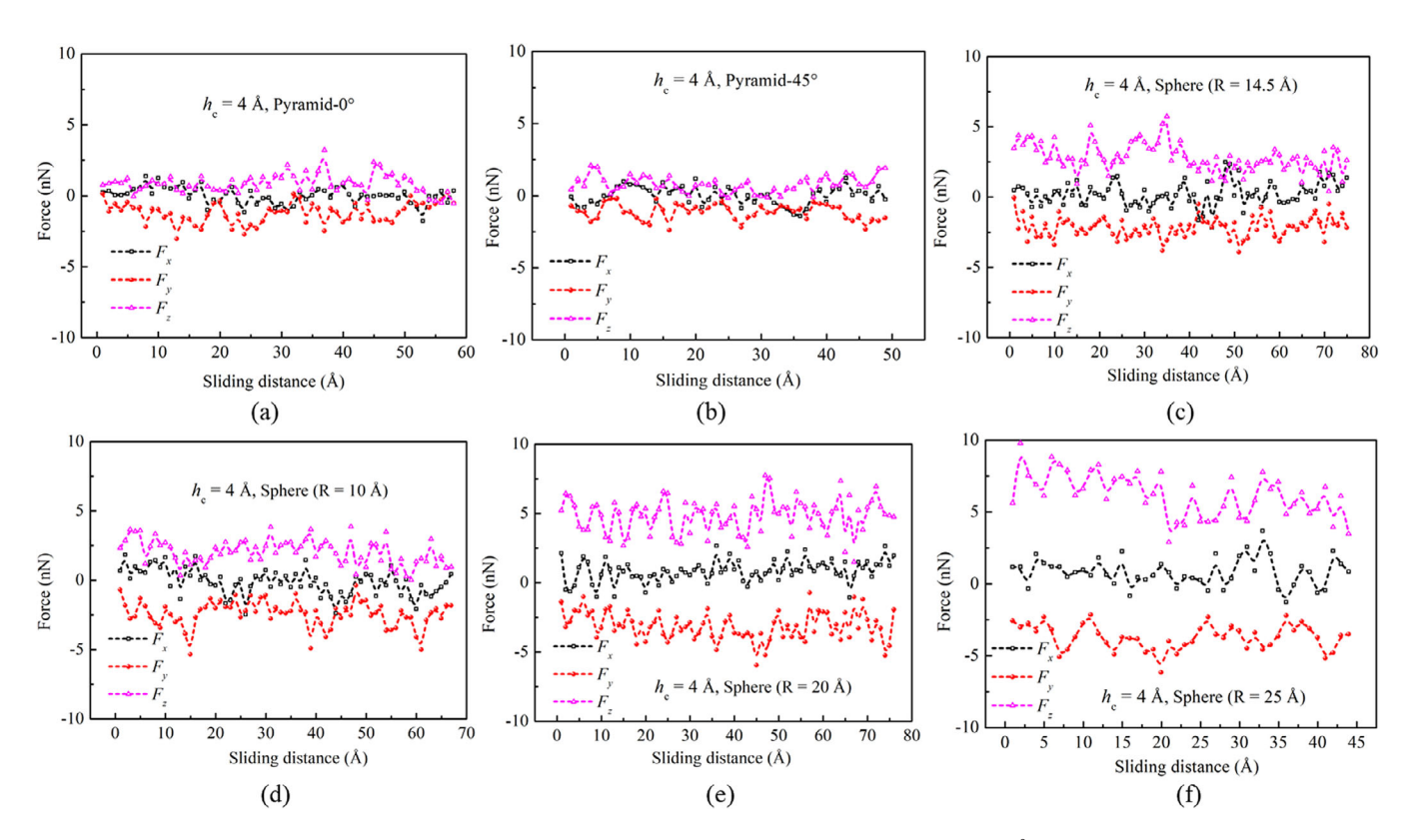


FIGURE 13 Evolution of the forces along three directions with sliding distance for all systems at h_c of 4 Å.

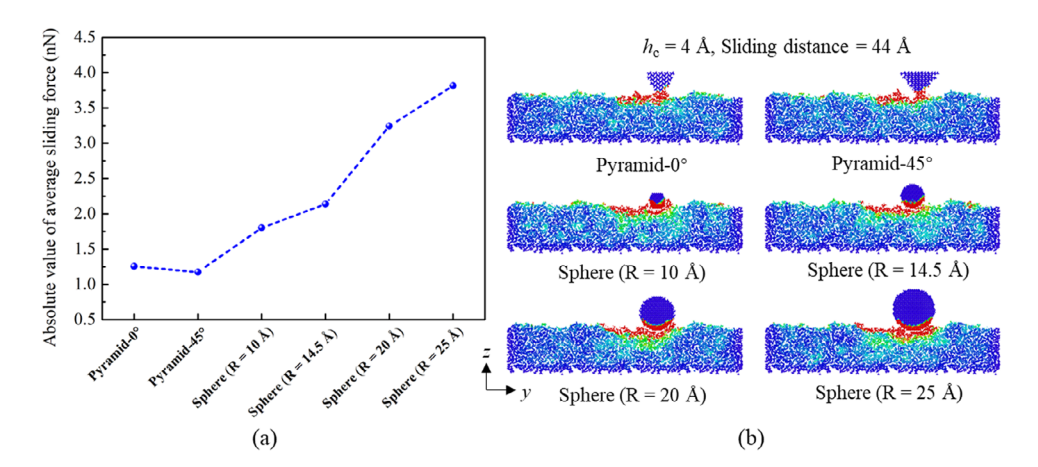


FIGURE 14 (a) The absolute value of the average sliding force is calculated based on the arithmetic average of the data at over 10 Å of the sliding distance. (b) Structural configuration of all systems at h_c of 4 Å and sliding distance of 44 Å.

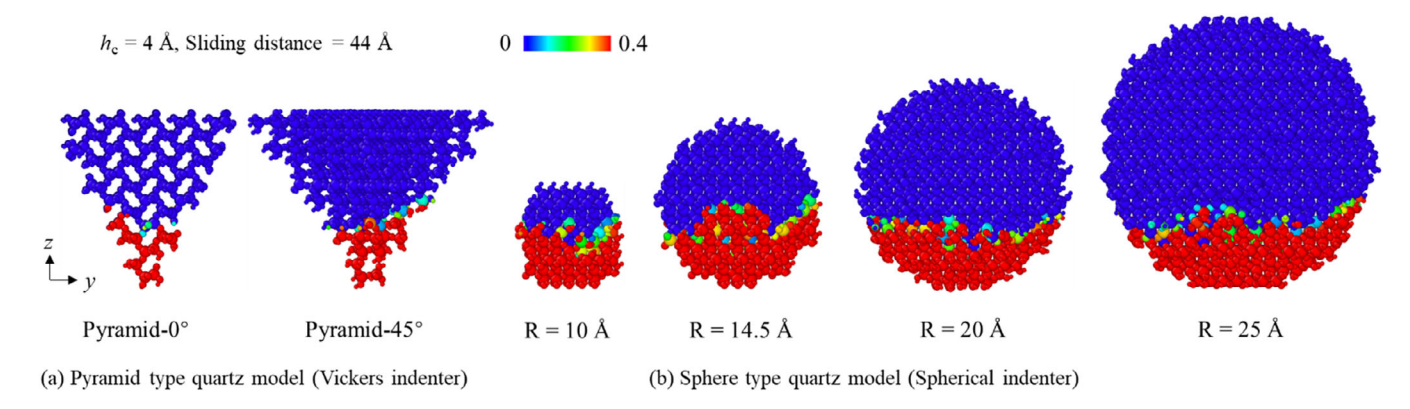


FIGURE 15 | Shear strain of atoms for all quartz indenters at h_c of 4 Å and sliding distance of 44 Å.

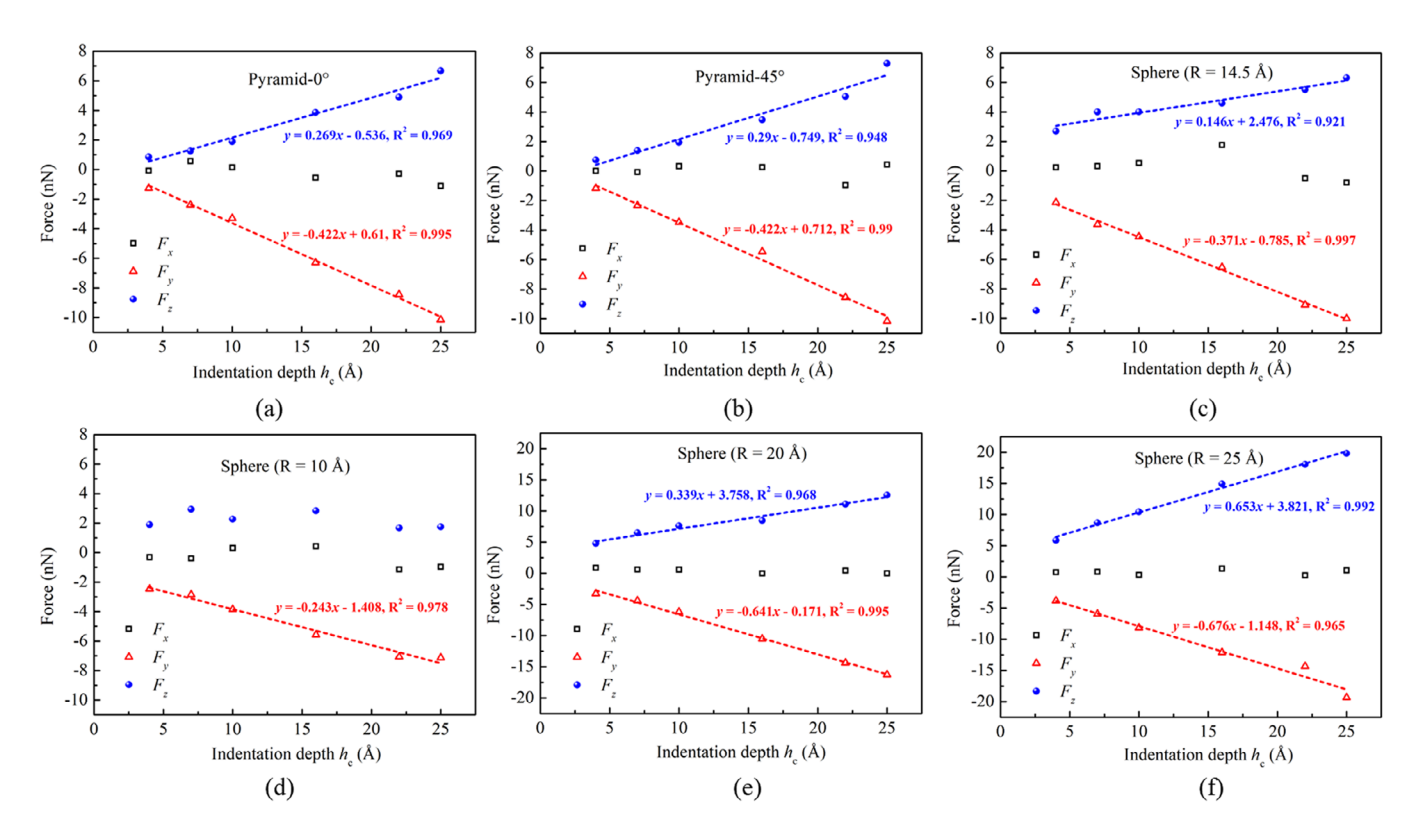


FIGURE 16 Evolution of forces along three directions with indentation depth (h_c) for all systems.

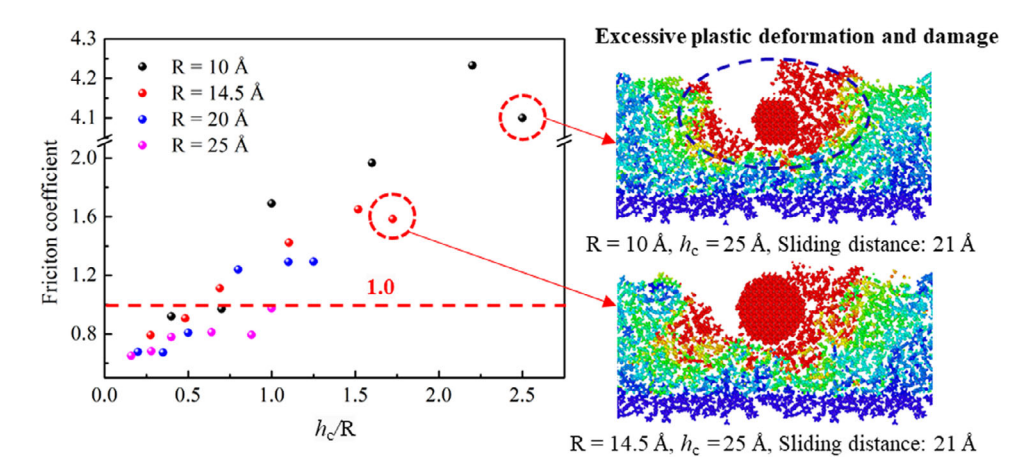


FIGURE 17 Evolution of the friction coefficient (F_v/F_z) with h_c/R for various spherical quartz indenters (R = 10 - 25 Å).

(0.4–1.8) [53], nylon (1.0–2.0) [54], etc. Moreover, negative friction coefficients (<0) have been observed in superlubric graphite-hexagonal boron nitride heterojunctions [56]. The complex friction properties of materials are significantly related to a number of factors, such as surface roughness, adhesion effect, contact area, lubrication status, and external environmental factors, where the adhesion effect of materials at the microscale was particularly dominant (see Figure S3).

To sum up, the classic Coulomb's law of friction does not apply at the nano- and microscale [57–59]. The friction coefficient could increase with rising indentation depth or $h_{\rm c}/R$ during nanoscratching (Figure 17), which is mainly due to the adhesion effect between materials. For example, the surface atomic inter-

actions, the surface roughness of the epoxy substrate, and the surface interlocking effect between quartz and epoxy significantly increase with rising $h_{\rm c}/R$, resulting in a higher sliding force and friction coefficient.

3.3.2 | Mechanical Analysis Between Macro- and Microscales

There is a space and time scale difference between MD nanoindentation simulations and its experiments, the size in nanoindentation experiments being in the order of tens-hundreds times that of MD nanoindentation simulations due to the computational limitations [30]. Moreover, in MD simulations, the space scale of quartz models is usually \sim nm, and its crystal structure at the microscale is usually perfect. However, the size of real quartz particles is \sim μm to mm, containing polycrystalline defects, grain boundaries, and dislocations [60]. Thus, it is necessary to develop cross-scale research methods to explore the multiscale mechanical behavior of these materials.

This study focuses on the atomic-level interaction mechanism of the quartz–epoxy interface, and the MD simulation results could provide basic input for the construction of larger-scale (e.g., $\sim \mu m$) contact models, such as the coarse-grained molecular dynamics (CGMD) approach [61]. On the one hand, this work can provide key microscopic insights and existing mechanisms, but it cannot be directly applied to geotechnical engineering [62, 63]. On the other hand, the modeling of the macroscopic mechanical response of the soil–FRP system requires an upscaling method, which could integrate microscopic mechanisms within a continuum approach, combining CGMD, discrete element method, and finite element method [64, 65].

3.3.3 | Future Works

Based on the findings of this study and previous works, several future works are worth conducting:

- As shown in Figure 6a, there is an adhesion effect between the epoxy substrate and the quartz indenter during the nanoindentation process. Virtual indenters could further elucidate the impact of this adhesion on MD nanoindentation and nanoscratching results by comparison to the effect of the quartz indenter.
- 2. The adhesive properties between soil and FRP will be essential for evaluating the interfacial properties of external factors, such as hydration, temperature, etc. Moreover, to increase the system's size and complexity, the periodic boundary conditions (PBCs) can be used in the *x* and *y*-directions for quartz and epoxy, as shown in Figure S4.
- 3. The methodologies and findings of this study apply not only to existing FRP materials but also to the evaluation and optimization of modified FRP materials. Thus, the mechanical properties of new high-performance geomaterials at the microscale could also be performed through MD nanoindentation and nanoscratching in the future.
- 4. Based on the discussion of Section 3.3.2, a multiscale correlation method of "microscopic mechanism—coarse-grained modeling—continuum mechanics" is worth developing, providing the multiscale insight and mechanism of material behavior.

4 | Conclusions

The MD simulation method was employed to investigate the quartz-indenter shape and indentation depth (h_c) effect on the interfacial mechanical behavior of epoxy through nanoindentation and nanoscratching, considering two Vickers-type and four spherical indenters with varying radii (R) under different h_c conditions. This work provided an atomistic insight into the

fundamental mechanisms governing the interfacial behavior of epoxy-quartz. The main conclusions are as follows:

- 1. During MD nanoindentation, the elastic–plastic deformation of epoxy and the indentation force (F_z) gradually increased with the indentation depth (h_c) and the radius of spherical indenter during the loading stage, due to the stronger interactions between the epoxy substrate and the quartz indenter. The plastic deformation zone expanded outward.
- 2. The values of reduced modulus (E_r) ranging from 1.84 to 6.17 GPa and Young's modulus (E) from 1.58 to 5.29 GPa for epoxy resin obtained in this work were consistent with previous experimental results.
- 3. The amorphous properties of epoxy resin resulted in the absence of a pop-in point during nanoindentation, aligning with previous experimental nanoindentation. Moreover, during the unloading stage, the negative value of F_z was due to the adhesion effect between epoxy and quartz, as verified by previous MD studies.
- 4. In MD nanoscratching, the absolute value of forces in the y-and z-directions could increase with increasing the radius of spherical quartz indenter and h_c , attributed to a larger contact zone and higher elastic–plastic deformation of epoxy.
- 5. For some spherical indenters, the friction coefficient could increase with rising indentation depth, exceeding 1.0 at $h_{\rm c}/R > 0.75$, which was mainly due to the adhesion effect and surface interlocking effect between quartz and epoxy. Moreover, the classic Coulomb's law of friction was not applicable at the microscale or nanoscale.

Author Contributions

Pengchang Wei: conceptualization, methodology, investigation, data curation, writing – review and editing, writing – original draft, visualization. **Zhen-Yu Yin**: conceptualization, writing – review and editing, supervision, project administration. **Pierre-Yves Hicher**: writing – review and editing, supervision. **Yuan-Yuan Zheng**: methodology, writing-review, and editing.

Acknowledgments

The authors thank the Research Grants Council (RGC) of Hong Kong Special Administrative Region Government (HKSARG) of China (Grant Number.: N_PolyU534/20, 15217220), Research Centre for Nature-based, Urban Infrastructure Solutions (Grant Number.: P0053045) of The Hong Kong Polytechnic University, and the Project of RCRE (Grant Number.: 1-BBEM) of The Hong Kong Polytechnic University for the support.

Conflicts of Interest

The authors declare no conflicts of interest.

Data Availability Statement

The analysis codes (i.e., calculating script in Lammps) used in this study for one epoxy-quartz system (i.e., spherical quartz-indenter with a radius of 25 Å, see Figure 1) could be obtained from https://github.com/weipc3/Nanoindentation-epoxy-quartz. Moreover, the more detailed data and code could be found in the Supporting Information.

References

- 1. M. Aliasghar-Mamaghani and A. Khaloo, "Effective Flexural Stiffness of Beams Reinforced With FRP Bars in Reinforced Concrete Moment Frames," *Journal of Composites for Construction* 25 (2021): 04020083.
- 2. J. Wan, A. Zaoui, X. Li, and Y. Zheng, "Molecular Dynamics Simulations of the Interface Friction Behavior Between Fiber-Reinforced Polymer Pile and Sand," *Tribology International* 192 (2024): 109288
- 3. W. Q. Xu, Z. Y. Yin, and Y. Y. Zheng, "FRP–Soil Interfacial Mechanical Properties With Molecular Dynamics Simulations: Insights Into Friction and Creep Behavior," *International Journal for Numerical and Analytical Methods* 47 (2023): 2951–2967.
- 4. M. Zappalorto, A. Pontefisso, A. Fabrizi, and M. Quaresimin, "Mechanical Behaviour of Epoxy/Silica Nanocomposites: Experiments and Modelling," *Composites Part A: Applied Science and Manufacturing* 72 (2015): 58–64.
- 5. M. Pando, G. Filz, J. Dove, and E. Hoppe, "Interface Shear Tests on FRP Composite Piles," in *International Deep Foundations Congress* (2002), 1486–1500.
- 6. H. A. Shaia, A. K. Al-Asadi, and S. H. Ramadan, "Evaluation of the Interface Friction Between Fiber-Reinforced Polymers and Granular Materials Using Modified Shear Apparatus," *International Journal of Civil Engineering and Technology* 9 (2018): 1010–1016.
- 7. M. J. Abyaneh, H. El Naggar, and P. Sadeghian, "Numerical Modeling of the Lateral Behavior of Concrete-Filled FRP Tube Piles in Sand," *International Journal of Geomechanics* 20 (2020): 04020108.
- 8. C. A. Anagnostopoulos and T. T. Papaliangas, "Experimental Investigation of Epoxy Resin and Sand Mixes," *Journal of Geotechnical and Geoenvironmental Engineering* 138 (2012): 841–849.
- 9. F. Gao, D. Stead, and D. Elmo, "Numerical Simulation of Microstructure of Brittle Rock Using a Grain-Breakable Distinct Element Grain-Based Model," *Computers and Geotechnics* 78 (2016): 203–217.
- 10. W. Zhu, J. J. Hughes, N. Bicanic, and C. J. Pearce, "Nanoindentation Mapping of Mechanical Properties of Cement Paste and Natural Rocks," *Materials Characterization* 58 (2007): 1189–1198.
- 11. Z. Ma, R. Pathegama Gamage, and C. Zhang, "Effects of Temperature and Grain Size on the Mechanical Properties of Polycrystalline Quartz," *Computational Materials Science* 188 (2021): 110138.
- 12. W. Yang, G. Ayoub, I. Salehinia, B. Mansoor, and H. Zbib, "The Effect of Layer Thickness Ratio on the Plastic Deformation Mechanisms of Nanoindented Ti/TiN Nanolayered Composite," *Computational Materials Science* 154 (2018): 488–498.
- 13. P. Wei, Z.-Y. Yin, C. Yao, Z. Ren, Y.-Y. Zheng, and W. Ma, "Atomistic Origin of Montmorillonite Clay Subjected to Freeze-Thaw Hysteresis," *Journal of Rock Mechanics and Geotechnical Engineering* (2024).
- 14. Q. Fan, Y. Zheng, D. Meng, Q. Guo, Y. Liu, and H. Wu, "Study on Improving the Performance of Engineered Cement-Based Composites by Modifying Binder System and Polyethylene Fiber/Matrix Interface," *Colloids and Surfaces A, Physicochemical and Engineering Aspects* 707 (2025): 135862.
- 15. Q. Fan, Y. Liu, Y. Zheng, D. Meng, Q. Guo, and Z. Hu, "The Microscopic Reinforcement Mechanism of Zhuhai Soft Soil by Cement-Based Stabilizer: From Microscopic Characterization to Molecular Dynamics Simulation," *Applied Surface Science* 681 (2025): 161574.
- 16. Y. Liu, Y.-Y. Zheng, H.-J. Lin, et al., "Calculation of Contact Angle via Young-Dupré Equation With Molecular Dynamic Simulation: Kaolinite as an Example," *Colloids and Surfaces A: Physicochemical and Engineering Aspects* 697 (2024): 134469.
- 17. W. Niu, Y. Zheng, Z. Yin, C. Yao, and P. Wei, "Multiscale Mechanical Behavior of Hydrated Expansive Soil: Insights From Experimental and MD Study," *Computers and Geotechnics* 181 (2025): 107129.

- 18. Y. L. Yaphary, Z. Yu, R. H. W. Lam, D. Hui, and D. Lau, "Molecular Dynamics Simulations on Adhesion of Epoxy-Silica Interface in Salt Environment," *Composites Part B: Engineering* 131 (2017): 165–172.
- 19. Y. Zamani Ketek Lahijania, M. Mohseni, and S. Bastani, "Characterization of Mechanical Behavior of UV Cured Urethane Acrylate Nanocomposite Films Loaded With Silane Treated Nanosilica by the Aid of Nanoindentation and Nanoscratch Experiments," *Tribology International* 69 (2014): 10–18.
- 20. M. Huang, K. Xu, C. Xu, G. Jin, and S. Guo, "Micromechanical Properties of Biocemented Shale Soils Analyzed Using Nanoindentation Test," *Journal of Geotechnical and Geoenvironmental Engineering* 147 (2021): 04021157.
- 21. B. Wang, W. Yang, J. Yao, Y. Zhang, and Z. Huang, "The Effects of Temperature and Indentation Parameters on Mechanical Properties of Calcite Through Molecular Dynamics Simulation," *Computers and Geotechnics* 177 (2025): 106835.
- 22. Z. Ma, C. Zhang, R. Pathegama Gamage, and G. Zhang, "Uncovering the Creep Deformation Mechanism of Rock-Forming Minerals Using Nanoindentation," *International Journal of Mining Science and Technology* 32 (2022): 283–294.
- 23. P. Frontini, S. Lotfian, M. A. Monclús, and J. M. Molina-Aldareguia, "High Temperature Nanoindentation Response of RTM6 Epoxy Resin at Different Strain Rates," *Experimental Mechanics* 55 (2015): 851–862.
- 24. H. Hu, W. Zhang, Y. Xing, and X. Li, "Molecular Dynamics Study on the Effect of Single Grain Boundary on the Mechanical Behavior of Alpha-Quartz," *International Journal of Rock Mechanics and Mining Sciences* (Oxford, England: 1997) 93 (2017): 94–100.
- 25. C. K. Lam and K. T. Lau, "Localized Elastic Modulus Distribution of Nanoclay/Epoxy Composites by Using Nanoindentation," *Composite Structures* 75 (2006): 553–558.
- 26. D. Tzetzis, G. Mansour, I. Tsiafis, and E. Pavlidou, "Nanoindentation Measurements of Fumed Silica Epoxy Reinforced Nanocomposites," *Journal of Reinforced Plastics and Composites* 32 (2013): 160–173.
- 27. M. R. Ayatollahi, S. Doagou Rad, and S. Shadlou, "Nano-/Microscale Investigation of Tribological and Mechanical Properties of Epoxy/MWNT Nanocomposites," *Macromolecular Materials and Engineering* 297 (2012): 689–701
- 28. M. Humood, A. Asif, T. Guin, K. Polychronopoulou, J. C. Grunlan, and A. A. Polycarpou, "Nanoindentation and Nanoscratch of Sub-Micron Polymer Nanocomposite Films on Compliant Substrate," *Thin Solid Films* 736 (2021): 138905.
- 29. P. Zhu, Y. Hu, H. Wang, and T. Ma, "Study of Effect of Indenter Shape in Nanometric Scratching Process Using Molecular Dynamics," *Materials Science and Engineering: A* 528 (2011): 4522–4527.
- 30. P. Wei, Z. Yin, P. Hicher, and W. Xu, "Interfacial Mechanical Behavior of Epoxy-Quartz: MD Nanoindentation and Nanoscratching Study," *Acta Geotechnica* 20 (2024): 1599–1620.
- 31. Y. Sun, L. Chen, L. Cui, Y. Zhang, and X. Du, "Molecular Dynamics Simulation of Cross-Linked Epoxy Resin and Its Interaction Energy With Graphene Under Two Typical Force Fields," *Computational Materials Science* 143 (2018): 240–247.
- 32. F. S. Emami, V. Puddu, R. J. Berry, et al., "Force Field and a Surface Model Database for Silica to Simulate Interfacial Properties in Atomic Resolution," *Chemistry of Materials* 26 (2014): 2647–2658.
- 33. D. Frenkel and B. Smit, *Understanding Molecular Simulation: From Algorithms to Applications* (Academic Press, 2001).
- 34. S. Plimpton, "Fast Paraller Algorithms for Short-Range Molecular Dynamics," *Journal of Computational Physics* 117 (1995): 1–19.
- 35. A. C. Fischer-Cripps, Nanoindentation, Vol. 1 (Springer Nature, 2011).
- 36. Z. Ma, R. P. Gamage, and C. Zhang, "Mechanical Properties of α -Quartz Using Nanoindentation Tests and Molecular Dynamics Simu-

- lations," International Journal of Rock Mechanics and Mining Sciences 147 (2021): 104878.
- 37. E. G. Herbert, G. M. Pharr, W. C. Oliver, B. N. Lucas, and J. L. Hay, "On the Measurement of Stress–Strain Curves by Spherical Indentation," *Thin Solid Films* 398–399 (2001): 331–335.
- 38. X. Ma, X. Kang, and J. Cao, "Origin of the Elastic Anisotropy of Silica Particles: Insights From First-Principles Calculations and Nanoindentation Molecular Dynamic Simulations," *Computers and Geotechnics* 159 (2023): 105489.
- 39. F. Shimizu, S. Ogata, and J. Li, "Theory of Shear Banding in Metallic Glasses and Molecular Dynamics Calculations," *Materials Transactions* 48 (2007): 2923–2927.
- 40. C. Qiu, P. Zhu, F. Fang, D. Yuan, and X. Shen, "Study of Nanoindentation Behavior of Amorphous Alloy Using Molecular Dynamics," *Applied Surface Science* 305 (2014): 101–110.
- 41. X. Du, H. Zhao, L. Zhang, et al., "Molecular Dynamics Investigations of Mechanical Behaviours in Monocrystalline Silicon due to Nanoindentation at Cryogenic Temperatures and Room Temperature," *Scientific Reports* 5 (2015): 16275.
- 42. W. J. Wright, G. Feng, and W. D. Nix, "A Laboratory Experiment Using Nanoindentation to Demonstrate the Indentation Size Effect," *Journal of Materials Education* 35 (2013): 135–143.
- 43. K. C. Bennett, L. A. Berla, W. D. Nix, and R. I. Borja, "Instrumented Nanoindentation and 3D Mechanistic Modeling of a Shale at Multiple Scales," *Acta Geotechnica* 10 (2015): 1–14.
- 44. K. Fu, Y. Chang, Y. Tang, and B. Zheng, "Effect of Loading Rate on the Creep Behaviour of Epoxy Resin Insulators by Nanoindentation," *Journal of Materials Science: Materials in Electronics* 25 (2014): 3552–3558.
- 45. S. Saseendran, M. Wysocki, and J. Varna, "Cure-State Dependent Viscoelastic Poisson's Ratio of LY5052 Epoxy Resin," *Advanced Manufacturing: Polymer & Composites Science* 3 (2017): 92–100.
- 46. M. Sánchez, J. Rams, M. Campo, A. Jiménez-Suárez, and A. Ureña, "Characterization of Carbon Nanofiber/Epoxy Nanocomposites by the Nanoindentation Technique," *Composites Part B: Engineering* 42 (2011): 638–644
- 47. C. R. Amaral, R. J. S. Rodriguez, F. G. Garcia, L. P. B. Junior, and E. A. Carvalho, "Impact of Aliphatic Amine Comonomers on DGEBA Epoxy Network Properties," *Polymer Engineering and Science* 54 (2014): 2132–2138.
- 48. A. Muller, J. S. Jang, J. Suhr, and R. F. Gibson, "Influence of Particle Diameter on Coefficient of Thermal Expansion of SiO2/Epoxy Particulate Composites," paper presented at the Process SAMPE Fall Technology Conference, Salt Lake City, October 11-14, 2010.
- 49. I. Oral, H. Guzel, and G. Ahmetli, "Determining the Mechanical Properties of Epoxy Resin (DGEBA) Composites by Ultrasonic Velocity Measurement," *Journal of Applied Polymer Science* 127 (2013): 1667–1675.
- 50. U. A. Samad, M. A. Alam, A. Chafidz, S. M. Al-Zahrani, and N. H. Alharthi, "Enhancing Mechanical Properties of Epoxy/Polyaniline Coating With Addition of ZnO Nanoparticles: Nanoindentation Characterization," *Progress in Organic Coatings* 119 (2018): 109–115.
- 51. J. Ren, J. Zhao, Z. Dong, and P. Liu, "Molecular Dynamics Study on the Mechanism of AFM-Based Nanoscratching Process With Water-Layer Lubrication," *Applied Surface Science* 346 (2015): 84–98.
- 52. S. J. Lee and C. L. Kim, "Influence of Surface Structure on Friction and Wear Characteristics of Silicone Rubber for Hydraulic Rod Seals," *RSC Advances* 13 (2023): 33595–33602.
- 53. I. Nitta, T. Masuda, and Y. Tsukiyama, "Elucidation of Frictional Properties Between Rubber and Flooring Using a Laser Microscope With Wide Field of View," *Tribology International* 174 (2022): 107775.
- 54. M. Watanabe, M. Karasawa, and K. Matsubara, "The Frictional Properties of Nylon," *Wear* 12 (1968): 185–191.

- 55. M. Jahanshahi, R. Mofidian, S. S. Hosseini, and M. Miansari, "Investigation of Mechanical Properties of Granular γ -Alumina Using Experimental Nano Indentation and Nano Scratch Tests," *SN Applied Sciences* 5 (2023): 164.
- 56. D. Mandelli, W. Ouyang, O. Hod, and M. Urbakh, "Negative Friction Coefficients in Superlubric Graphite-Hexagonal Boron Nitride Heterojunctions," *Physical Review Letters* 122 (2019): 76101–76102.
- 57. P. Wei, S. Zhou, Y. Zheng, Z. Yin, and W. Xu, "Nanoscale Stick-Slip Behavior and Hydration of Hydrated Illite Clay," *Computers and Geotechnics* 166 (2024): 105976.
- 58. Z. He, Y. Zheng, Z. Yin, and P. Wei, "Nanoscale Interfacial Tribology Behavior Between Clay and Sand: Effects of Cations, Normal Load and Sliding Velocity," *Acta Geotechnica* 20 (2025): 2761-2778.
- 59. P. Stoyanov and R. R. Chromik, "Scaling Effects on Materials Tribology: From Macro to Micro Scale," *Materials* 10 (2017): 550.
- 60. H. Kemnitz and B. Lucke, "Quartz Grain Surfaces; a Potential Microarchive for Sedimentation Processes and Parent Material Identification in Soils of Jordan." *Catena (Giessen)* 176 (2019): 209–226.
- 61. H. Zhu, A. J. Whittle, and R. J. Pellenq, "Potential of Mean Force for Face-Face Interactions Between Pairs of 2:1 Clay Mineral Platelets," *Langmuir* 38 (2022): 13065–13074.
- 62. X. Liu, S. Jiang, J. Xie, and X. Li, "Bayesian Inverse Analysis With Field Observation for Slope Failure Mechanism and Reliability Assessment Under Rainfall Accounting for Nonstationary Characteristics of Soil Properties," *Soils Found* 65 (2025): 101568.
- 63. X. Liu, X. Li, G. Ma, and M. Rezania, "Characterization of Spatially Varying Soil Properties Using an Innovative Constraint Seed Method," *Computers and Geotechnics* 183 (2025): 107184.
- 64. P. Wang, Z. Yin, W. Zhou, and W. Chen, "Micro-mechanical Analysis of Soil-Structure Interface Behavior Under Constant Normal Stiffness Condition With DEM," *Acta Geotechnica* 17 (2022): 2711–2733.
- 65. P. Wang, Z. Y. Yin, P. Y. Hicher, and Y. J. Cui, "Micro-Mechanical Analysis of One-Dimensional Compression of Clay With DEM," *International Journal for Numerical and Analytical Methods* 47 (2023): 2706–2724.

Supporting Information

Additional supporting information can be found online in the Supporting Information section.

Supporting File 1: nag4021-sup-0001-SuppMat.docx. Supporting File 2: nag4021-sup-0002-VidS1.mp4. Supporting File 3: nag4021-sup-0003-VidS2.mp4. Supporting File 4: nag4021-sup-0004-VidS3.mp4. Supporting File 5: nag4021-sup-0005-VidS4.mp4. Supporting File 6: nag4021-sup-0006-VidS5.mp4. Supporting File 7: nag4021-sup-0007-VidS6.mp4. Supporting File 8: nag4021-sup-0008-Data.zip